

Supplementary Information for:

Impact of the water-compatible periphery on the dynamic and structural properties of benzene-1,3,5-tricarboxamide based amphiphiles

*S.M.C. Schoenmakers,^a C.M.A. Leenders,^a R.P.M. Lafleur,^a X. Lou,^a E.W. Meijer,^{*a} G.M. Pavan^{*b} and A.R.A. Palmans^{*a}*

^a Institute for Complex Molecular Systems, Eindhoven University of Technology, P.O. Box 513, 5600 MB Eindhoven, The Netherlands. E-mail: a.palmans@tue.nl. Tel: +31 040 2473105

^b Department of Innovative Technologies, University of Applied Sciences and Arts of Southern Switzerland, Galleria 2, Via Cantonale 2c, Manno CH-6928, CH. Email: giovanni.pavan@supsi.ch

Table of Contents:

1. Materials and Methods	S2
2. Supplementary figures	S6
Fig. S1	S6
Fig. S2	S6
Fig. S3	S7
Fig. S4	S7
Fig. S5	S8
Fig. S6	S9
Fig. S7	S10
Fig. S8	S11
Fig. S9	S12
Fig. S10	S13
Fig. S11	S13
Fig. S12	S14
Fig. S13	S14
Fig. S14	S15
3. HDX-MS measurements	S16
Fig. S15	S18
Fig. S16	S19
4. Molecular dynamics simulations	S20
5. References	S21

1. Materials and methods:

Materials: EG-BTA¹ and Glu-BTA² were synthesized according to literature procedures. Water was purified on an EMD Millipore Milli-Q Integral Water Purification System. Toluene and methanol were of spectroscopic grade.

Sample preparation procedure: All BTA samples were prepared in MQ-water, which was first filtered with a 0.2 µm syringe filter (Supor membrane, Pall Corporation). EG-BTA samples were prepared by adding the solid material to a glass vial, adding MQ-water to obtain the desired concentration, stirring the sample at 80 °C for 15 minutes and by vortexing the sample for 15 seconds immediately afterwards. Glu-BTA samples were prepared by adding the solid material to a glass vial, adding MQ-water to obtain the desired concentration and stirring the sample at 70 °C for 15 minutes and by vortexing the sample for 15 seconds immediately afterwards. All samples were left to equilibrate overnight before being used for any measurements.

Samples in methanol were prepared by adding the solid material to a glass vial, adding methanol to obtain the desired concentration and letting the sample equilibrate overnight.

Static light scattering measurements were recorded on an ALV/CGS-3 MD-4 compact goniometer system equipped with a multiple tau digital real time correlator (ALV-7004) and a solid state laser ($\lambda = 532$ nm; 40 mW). Scattering intensity was detected over an angular range of 30° to 150° with steps of 5°, and averaged over at least 4 runs of 10 seconds per angle. BTA samples were prepared at a concentration of 582 µM and were measured in light scattering tubes with an outer diameter of 1 cm. As a reference, samples of only the corresponding solvent and only toluene were measured. Water was filtered with a 0.2 µm syringe filter (Supor membrane, PALL Corporation) and methanol and toluene were filtered with a 0.2 µm syringe filter (PTFE membrane, Whatman). The measurements were analysed with AfterALV (1.0d, Dullware) to remove measurements showing obvious scattering from dust. The Rayleigh ratio as a function of the angle was computed using the equation below with toluene as a reference:

$$R_{\theta} = \frac{I_{\text{sample}} - I_{\text{solvent}}}{I_{\text{toluene}}} \times R_{\text{toluene}} \times \frac{n_{\text{solvent}}^2}{n_{\text{toluene}}^2}$$

(1)

with I_{sample} the count rate of the sample solution, I_{solvent} the count rate for the solvent (water or methanol) and I_{toluene} the count rate for toluene. R_{toluene} is the known Rayleigh ratio of toluene ($2.1 \times 10^{-2} \text{ m}^{-1}$ at 532 nm)³, n_{solvent} is the refractive index of the solvent (1.333 for water, 1.331 for methanol) and n_{toluene} is the refractive index of toluene (1.497). For measurements at higher temperatures, the samples were first equilibrated at 75 °C for at least 2 hours before the temperature was decreased to the desired temperature. The samples were equilibrated for another 30 minutes at the desired temperature before the measurement was started.

Cryogenic transmission electron microscopy was performed on samples with a concentration of 0.75 mg/mL. Vitrified films were prepared in a ‘Vitrobot’ instrument (PC controlled vitrification robot, patent applied, Frederik et al 2002, patent licensed to FEI) at 22°C and a humidity of 100%. In the preparation chamber of the ‘Vitrobot’ a 3 μL sample was applied on a Quantifoil grid (R 2/2, Quantifoil Micro Tools GmbH), which was surface plasma treated just prior to use (Cressington 208 carbon coater operating at 5 mA for 40 s). Excess sample was removed by blotting using filter paper for 2s at –2 mm, and the thin film thus formed was shot (acceleration about 3 g) into liquid ethane just above its freezing point. The vitrified film was transferred to a cryoholder (Gatan 626) and observed at –170 °C in a Tecnai Sphera microscope operating at 200 kV. Microscopy images were taken at low dose conditions and at a defocus of 10 μm (magnification: 25000).

Fourier-Transform infrared (FT-IR) spectra were recorded on a Perkin Elmer Spectrum Two FT-IR spectrometer. Solution FT-IR measurements were performed using a CaF_2 Liquid Cell with an optical path length of 0.05 mm. For the solution samples, first a background of the appropriate solvent was measured. All spectra were measured at room temperature from 400 cm^{-1} to 4000 cm^{-1} and were averaged over 64 scans. Samples for FT-IR were prepared at a concentration of 50 mg/mL **EG-BTA** and at a concentration of 20 mg/mL for **Glu-BTA** to facilitate dissolution. BTA material was weighed and added to a clean vial. All samples were dried overnight with approximately 5 grams of P_2O_5 in a separate beaker in the vacuum oven at 40 °C. MeOD was added to the vials to obtain the desired concentration. Samples in D_2O were prepared by stirring the samples at 80 °C for 15 minutes after adding the solvent to obtain the desired concentration. The hot and hazy were subsequently vortexed for 15 seconds and this procedure was repeated again if the sample looked still hazy. All samples were left to equilibrate at room temperature overnight and were viscous the next day.

Ultraviolet-visible (UV-vis) absorbance spectra were recorded on a Jasco V-650 UV-Vis spectrometer equipped with a Jasco ETCT-762 temperature controller or on a Jasco V-750 UV-Vis spectrometer equipped with a PAC-743 multi-cuvette holder and Jasco ETCT-762 temperature controller. Measurements were performed using Quartz cuvettes with a pathlength of 1 mm (500 μ M samples), 1 cm (50 μ M samples) or 5 cm (5 μ M samples). First, a baseline of the corresponding solvent was measured. All samples were equilibrated for at least 30 minute at each temperature before starting the measurement. All measurements were performed with a bandwidth of 1.0 nm, a scan speed of 100 nm/min and a data interval of 0.1 nm, spanning the UV-Vis range from 350 nm to 190 nm. All spectra were averaged over three measurements.

Temperature dependent UV-vis absorbance spectra were recorded on a Jasco V-750 UV-Vis spectrometer equipped with a PAC-743 multi-cuvette holder and Jasco ETCT-762 temperature controller. Measurements were done in Quartz cuvettes with a pathlength of 1 cm. The measurements were done with a bandwidth of 1.0 nm, a response of 0.96 s and were recorded at 225 nm and 340 nm. Heating-cooling programs with a temperature ramp of 0.2 $^{\circ}$ C/min were used and spectra were created by sampling every 0.5 $^{\circ}$ C. The cloud point of **EG-BTA** was defined as the inflection point of the curve, obtained from the maximum of the derivative of the absorbance-temperature curve (Fig. S5C).⁴

Nuclear magnetic resonance spectra were recorded on Bruker 400 MHz Ultrashield spectrometers (400 MHz for 1 H NMR). Deuterated solvents used are indicated in each case. Chemical shifts (δ) are expressed in ppm values relative to tetramethylsilane. Peak multiplicity is abbreviated as s: singlet; d: doublet; t: triplet; q: quartet; m: multiplet.

Variable temperature 1 NMR spectra were recorded on a 500 MHz Varian Unit Inova using and D₂O as a solvent and to set the peak positions. All samples were equilibrated at a specific temperature for 30 minutes before the measurements were started. The spectra were averaged over 256 scans.

Fluorescence measurements with Nile Red were recorded on a Varian Cary Eclipse fluorescence spectrometer. A cuvette with an optical path length of 1 cm was used and the temperature was set at 20 $^{\circ}$ C. The sample was excited at 500 nm and the emission was recorded at 520-800 nm with a PMT detector voltage of 800 V. Each measurement was averaged over 5 scans. Samples for fluorescence measurements were prepared at a concentration of 50 μ M BTA

in water. A Nile Red stock solution with a concentration of 2.5 mM in ACN was diluted 10 times with ACN to a concentration of 0.25 mM. 5 μL of this stock solution was added to 495 μL of the BTA sample to obtain a concentration of 2.5 μM Nile Red in a 50 μM BTA sample. The samples were left to equilibrate at room temperature for 1 hour before the measurements.

Hydrogen/Deuterium Exchange (HDX) followed by mass spectrometry measurements were carried out using a XevoTM G2 QToF mass spectrometer (Waters) with a capillary voltage of 2.7 kV, a cone voltage of 80 V and an extraction cone voltage of 4.0 V. The source temperature was set at 100°C, the desolvation temperature at 400°C, and the cone gas flow at 10 L/h and the desolvation gas flow at 500 L/h. BTA samples were diluted with D₂O (including 0.5 mM sodium acetate to facilitate detection) to a concentration of 5 μM using a balance. Aliquots of these 5 μM samples were taken at specific time points and were subjected to ESI-MS. The sample solutions subjected to H/D exchange were introduced into the mass spectrometer using a Harvard syringe pump (11 Plus, Harvard Apparatus) at a flow rate of 50 $\mu\text{L}/\text{min}$. All samples were stored at room temperature during the course of the HDX-MS experiments. Before each measurement, the system was calibrated with a 0.05% H₃PO₄ solution in 1:1 H₂O:ACN. Samples were injected with a syringe pump and the signal was left to equilibrate for 1 minute before starting the measurement. Each measurement was averaged over 1 minute to account for instabilities in the signal. Isotope patterns for calculation were determined with Bruker Compas IsotopePattern software.

2. Supplementary Figures

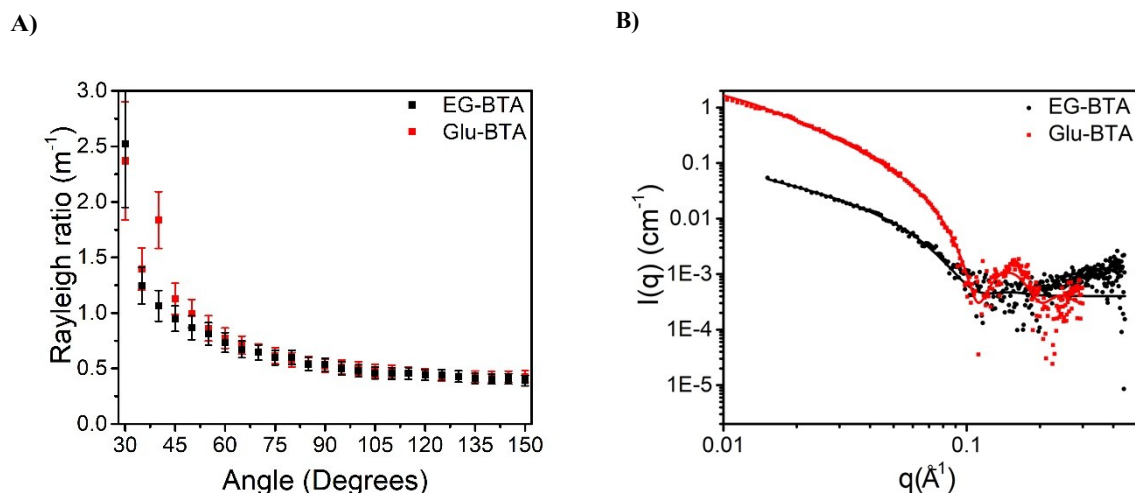


Fig. S1 (A) Rayleigh ratio as a function of the angle for assemblies of **EG-BTA** and **Glu-BTA** in H₂O ($c = 582 \mu\text{M}$, $\lambda = 532 \text{ nm}$). The angle dependence of the Rayleigh ratio indicates the presence of anisotropic assemblies and the overlapping profiles indicate that the assemblies are of the same dimensions. The squares represent the average Rayleigh ratio and the error bars represent the standard deviation calculated from at least four measurements. (B) SAXS profiles of **EG-BTA**⁵ (3.5 mM) and **Glu-BTA**² (3.2 mM) in aqueous solutions ($l = 2 \text{ mm}$, $\lambda = 532 \text{ nm}$, $T = 20 \text{ }^\circ\text{C}$). Both profiles could be fitted to a wormlike chain model⁶, yielding a contour length beyond the accessible limit and a cross-sectional radius of $3.1 \pm 0.02 \text{ nm}$ for assemblies of **EG-BTA** and $3.4 \pm 0.01 \text{ nm}$ for assemblies of **Glu-BTA**.

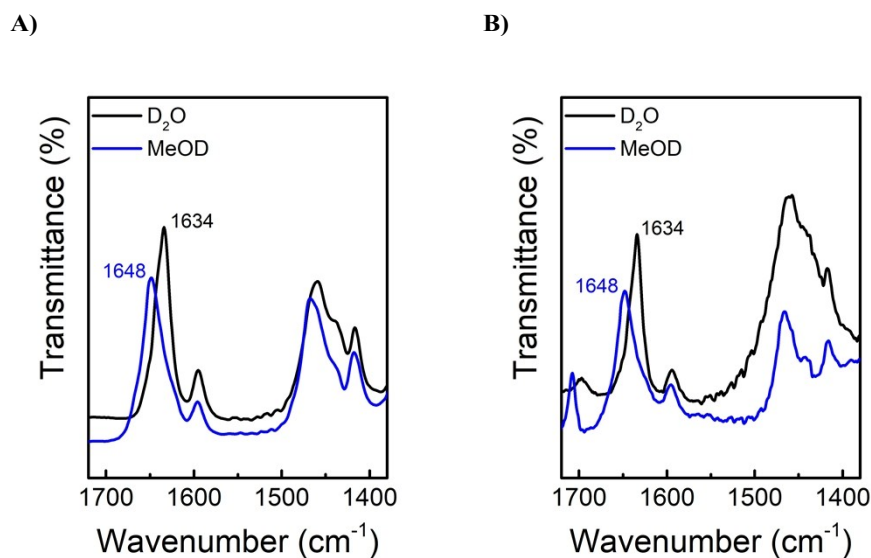


Fig. S2 Zoom of the amide I vibration in the FT-IR spectra of (A) **EG-BTA** ($c = 50 \text{ mg/mL}$, $T = \text{room temperature}$, $l = 0.05 \text{ mm}$) and (B) **Glu-BTA** ($c = 20 \text{ mg/mL}$, $T = \text{room temperature}$, $l = 0.05 \text{ mm}$) in D₂O and MeOD. The BTAs are molecularly dissolved in MeOD resulting in an amide I vibration at 1648 cm^{-1} for both molecules. The amide I vibration is positioned at 1634 cm^{-1} when the BTAs are assembled in D₂O. As reported before, this position is indicative for the presence of intermolecular hydrogen bonds stabilising the fibers.⁷ When compared to the spectrum in MeOD, it can be concluded that intermolecular hydrogen bonds between the core amide groups are present in assemblies of **EG-BTA** and **Glu-BTA** in aqueous solutions.

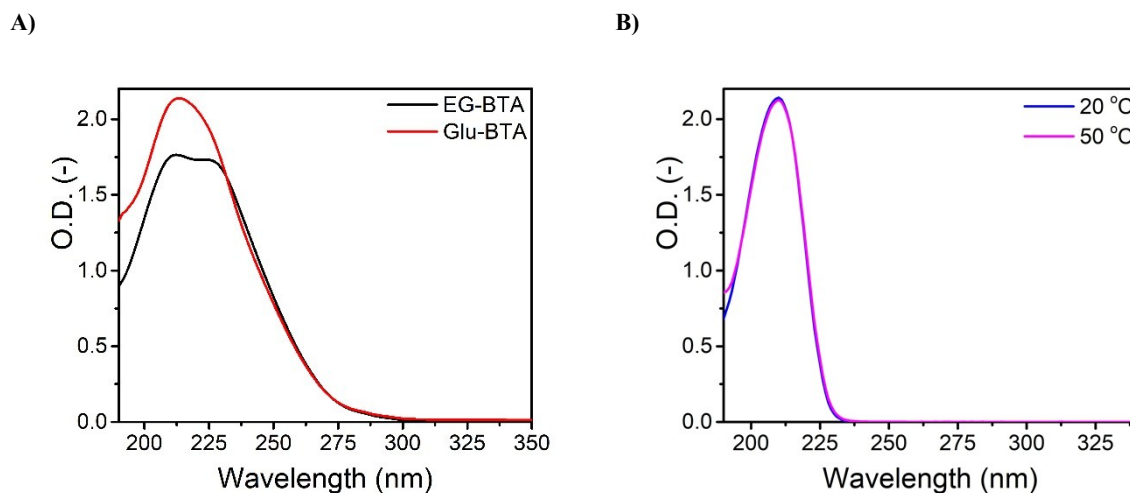


Fig. S3 (A) UV-Vis spectrum of **EG-BTA** and **Glu-BTA** in H₂O ($c = 500 \mu\text{M}$, $l = 1 \text{ mm}$, $T = 20 \text{ }^\circ\text{C}$). (B) UV-Vis spectrum of a solution of 1,2,3-triazole in H₂O ($c = 100\mu\text{M}$, $l = 1 \text{ cm}$) at $20 \text{ }^\circ\text{C}$ and $50 \text{ }^\circ\text{C}$. It is shown that the triazole moiety absorbs light at the same wavelength as **Glu-BTA**. No temperature dependence in the absorbance of the triazole moiety was observed.

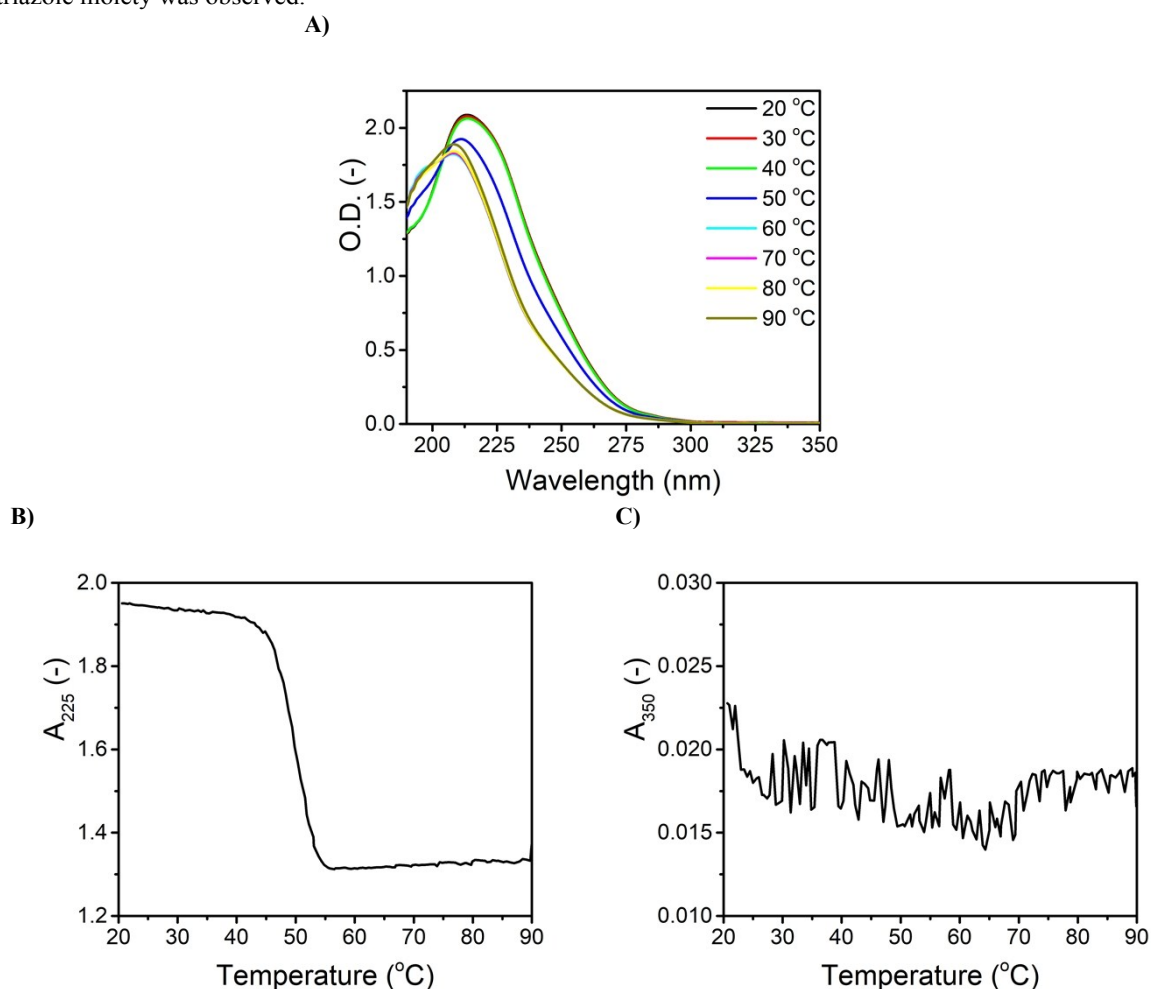


Fig. S4 (A) UV-Vis spectra of **Glu-BTA** at different temperatures when cooling down from $90 \text{ }^\circ\text{C}$ to $20 \text{ }^\circ\text{C}$ in water ($c = 50 \mu\text{M}$, $l = 1 \text{ cm}$). In contrast to **EG-BTA** no increase in the absorbance at high wavelengths at high temperature is observed, indicating that no large aggregates are formed until $90 \text{ }^\circ\text{C}$. (B) UV absorbance at 225 nm as a function of decreasing temperature for **Glu-BTA** in water (temperature ramp = $0.2 \text{ }^\circ\text{C}/\text{min}$, $c = 50 \mu\text{M}$, $l = 1 \text{ cm}$), revealing a transition in the UV absorbance from $55 \text{ }^\circ\text{C}$ to $43 \text{ }^\circ\text{C}$ which is further studied in Fig. S6 and S7. (C) UV cooling trace at 350 nm as a function of decreasing temperature for **Glu-BTA** in water (temperature ramp = $0.2 \text{ }^\circ\text{C}/\text{min}$, $c = 50 \mu\text{M}$, $l = 1 \text{ cm}$), showing that there is no cloud point temperature for those assemblies.

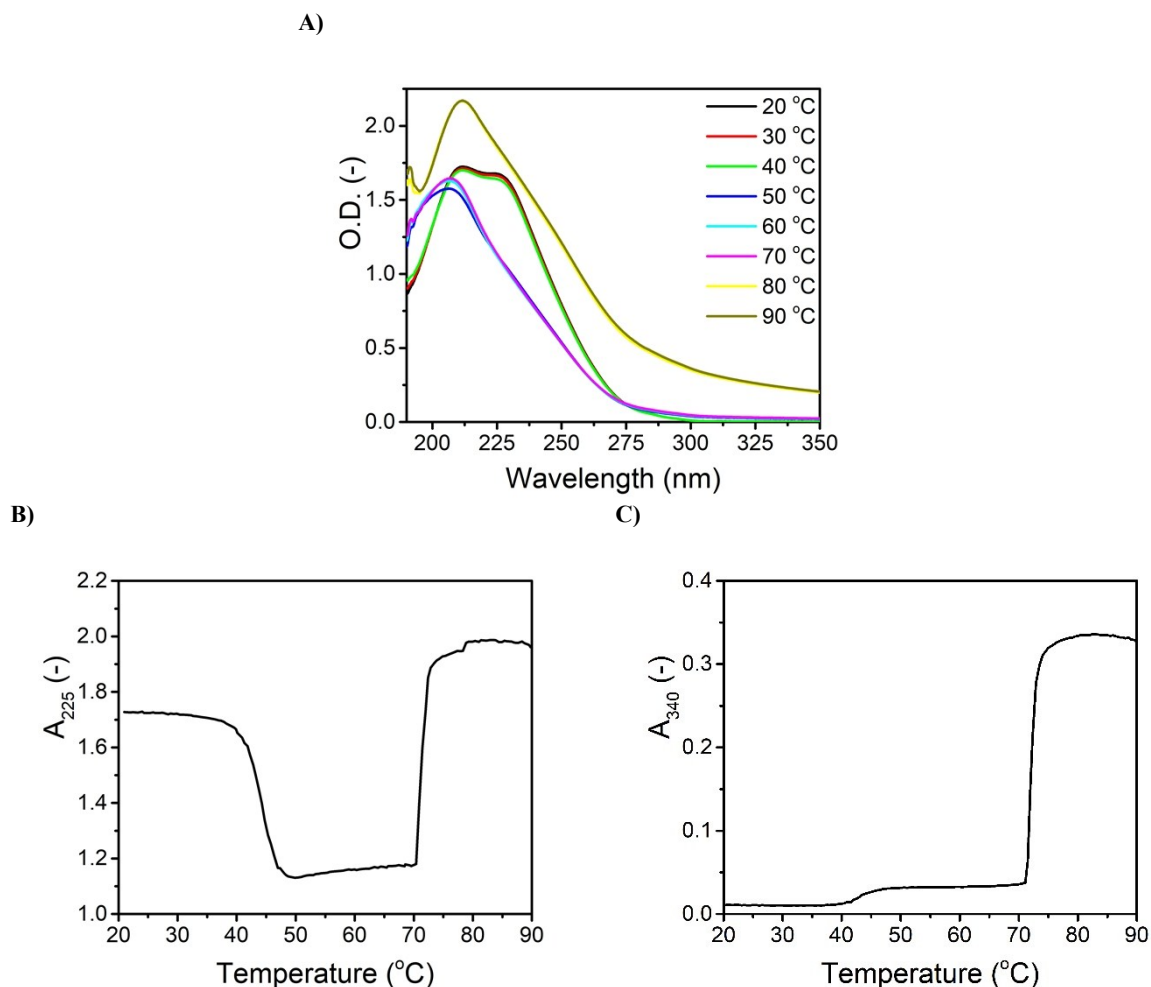
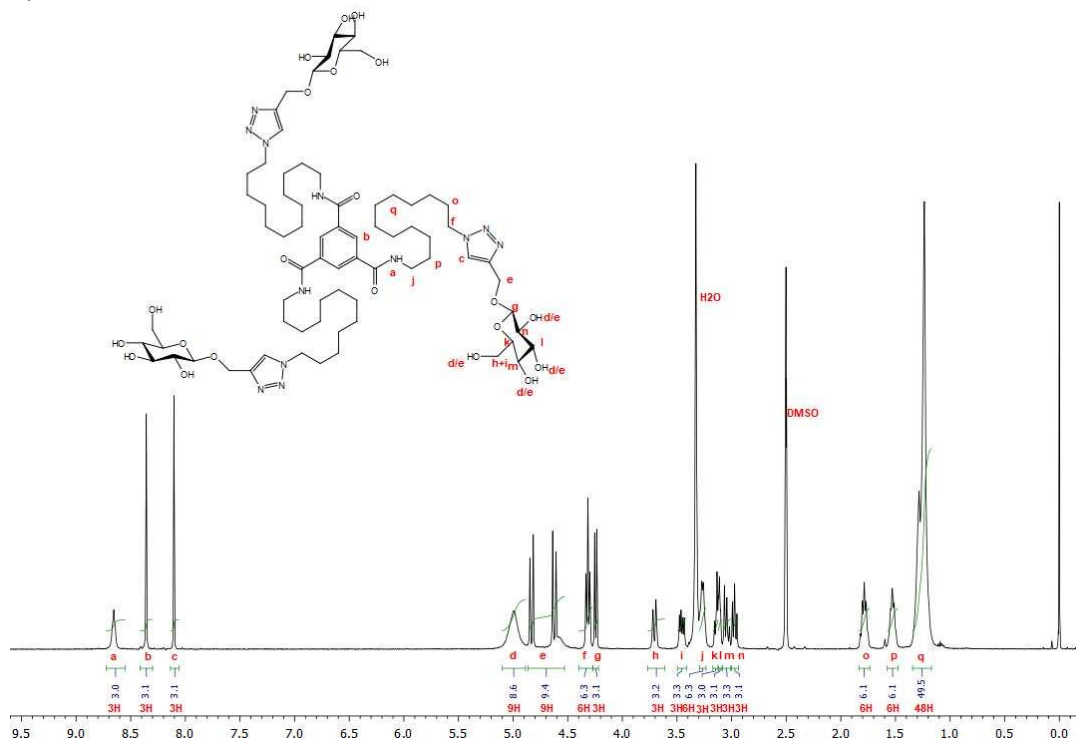


Fig. S5 (A) UV-Vis spectra of **EG-BTA** at different temperatures when cooling down from 90 °C to 20 °C in water ($c = 50 \mu\text{M}$, $l = 1 \text{ cm}$). A drastic increase in the UV-absorbance is found at higher wavelengths above 70 °C, indicating that large aggregates are formed at elevated temperatures. (B) UV absorbance at 225 nm as a function of decreasing temperature for **EG-BTA** in water (temperature ramp = 0.2 °C/min, $c = 50 \mu\text{M}$, $l = 1 \text{ cm}$), revealing a sharp transition around 72 °C and a transition from 50 °C to 38 °C. The transition at 72 °C corresponds to the T_{cp} (see (C)) and the origin of the transition from 50 °C to 38 °C is further investigated in Fig. S8 and S9. (C) UV cooling trace at 340 nm (at which there is normally no absorbance from the BTA chromophore) as a function of decreasing temperature for **EG-BTA** in water (temperature ramp = 0.2 °C/min, $c = 50 \mu\text{M}$, $l = 1 \text{ cm}$), showing a T_{cp} at 72 °C arising from the LCST behaviour of ethylene glycol. Additionally, a small transition at 45 °C is observed, overlapping with the cooperative transition observed in (B).

A)



B)

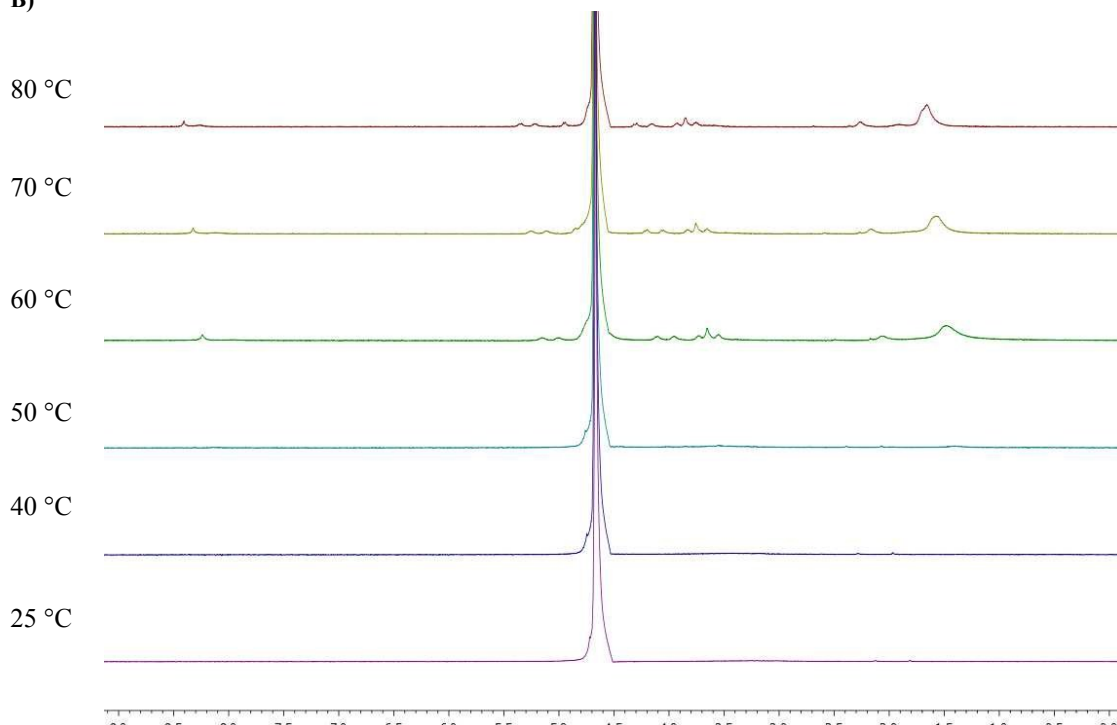
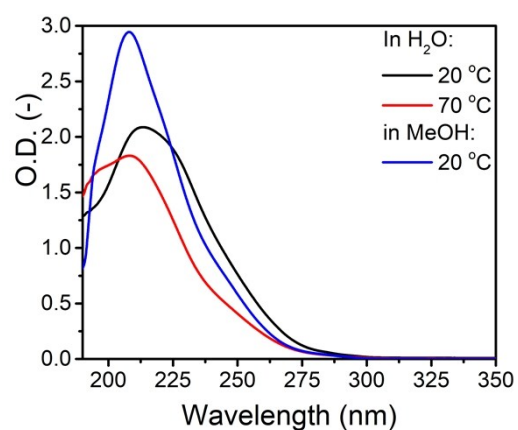


Fig. S6 $^1\text{H-NMR}$ (400 MHz) spectrum of **Glu-BTA** in $(\text{CD}_3)_2\text{SO}$. $\delta = 8.66$ (t, 3H, $\text{C}=\text{ONHCH}_2$), 8.36 (s, 3H, Ar), 8.10 (s, 3H, triazole), 5.00 (broad, 9H, pyranoside-OH), 4.73 (m, 9H, pyranoside-OH, triazole CH_2O), 4.31 (t, 6H, CH_2CH_2 triazole), 4.24 (d, 3H, triazole CH_2OCH), 3.71 (d, 3H, pyranoside $\text{C}_6\text{H}_2\text{OH}$), 3.46 (m, 3H, pyranoside $\text{C}_6\text{H}_2\text{OH}$), 3.27 (q, 6H, $\text{C}=\text{ONHCH}_2$), 3.13 (m, 3H, pyranoside C_3H), 3.11 (m, 3H, pyranoside $\text{C}_5\text{HCH}_2\text{OH}$), 3.05 (m, 3H, pyranoside C_4H), 2.97 (t, 3H, pyranoside C_2H), 1.79 (p, 6H, CH_2CH_2 triazole), 1.55 (p, 6H, $\text{C}=\text{ONHCH}_2\text{CH}_2$), 1.26 (m, 48H, aliphatic). (B) Variable temperature $^1\text{H-NMR}$ (500 MHz) of **Glu-BTA** when cooling down from 80 °C to 25 °C in D_2O ($c = 500 \mu\text{M}$). The signal at 4.79 ppm corresponds to D_2O . At 80 °C broad peaks corresponding to the aliphatic chain (around 1.7 ppm) and saccharide end groups and a small peak for the aromatic region (around 8.5 ppm) are present. When cooling down to 60 °C the peaks gradually shift upfield and they become broader. At 50 °C all peaks have disappeared, indicating that large aggregates have formed in solution.

A)



B)

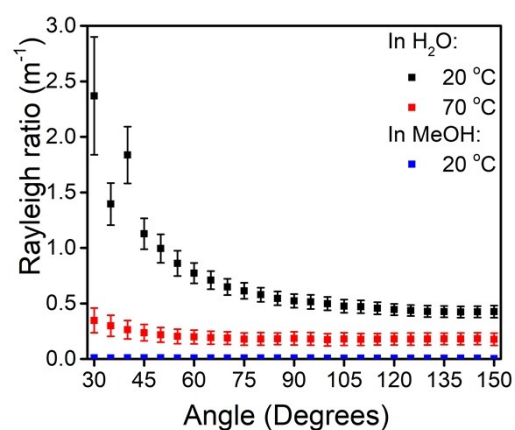
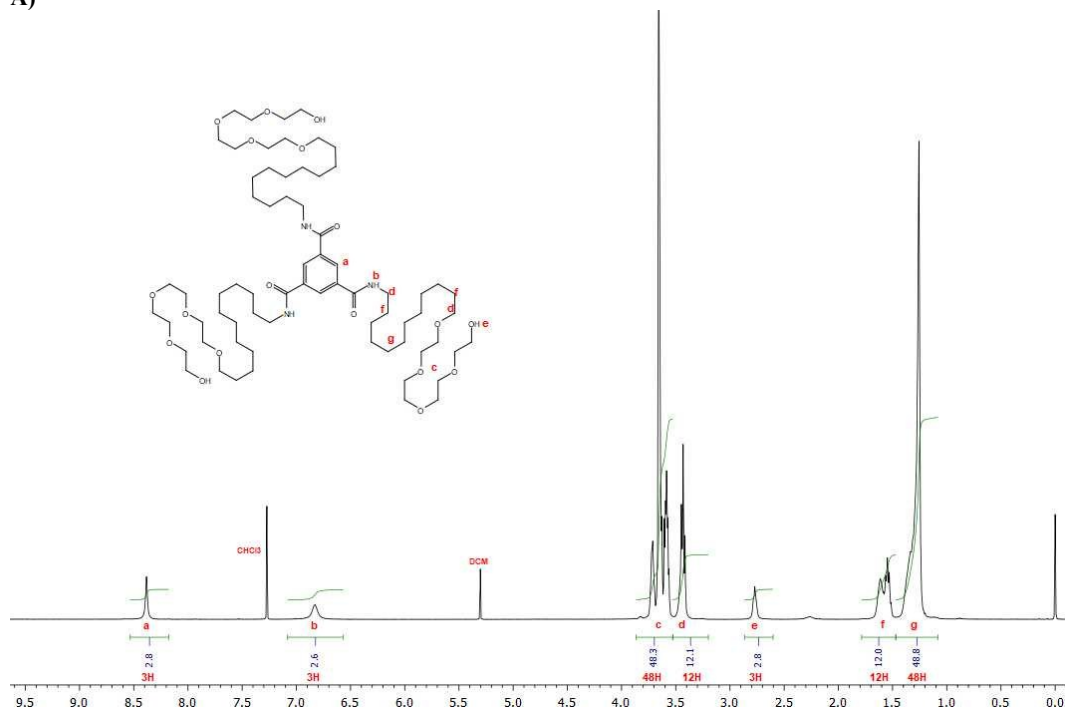


Fig. S7 The change in aggregation state at high temperatures observed for **Glu-BTA** in Fig. S4B was studied in more detail. (A) The UV-Vis spectrum of **Glu-BTA** ($c = 500 \mu\text{M}$, $l = 1\text{mm}$) at 70°C shows a large maximum at 209 nm , while this maximum shifts to 213 nm at 20°C . We hypothesized that this transition is the result of a change of the aggregation state from small aggregates or molecularly dissolved BTAs at 70°C to supramolecular polymers at 20°C . To study the presence of molecularly dissolved BTAs we recorded the UV-Vis spectrum of **Glu-BTA** in MeOH, a solvent in which the BTAs are molecularly dissolved, and found a maximum at 208 nm with higher absorbance than in H₂O at 70°C . This already suggests that **Glu-BTA** is not molecularly dissolved at 70°C . (B) SLS of **Glu-BTA** ($c = 582 \mu\text{M}$, $\lambda = 532\text{ nm}$) at 70°C shows an angle-dependent Rayleigh ratio. When **Glu-BTA** is molecularly dissolved in MeOH, the Rayleigh ratio is significantly lower and there is no angle dependence. These results show that **Glu-BTA** is not molecularly dissolved at 70°C but it forms small non-spherical aggregates.

A)



B)

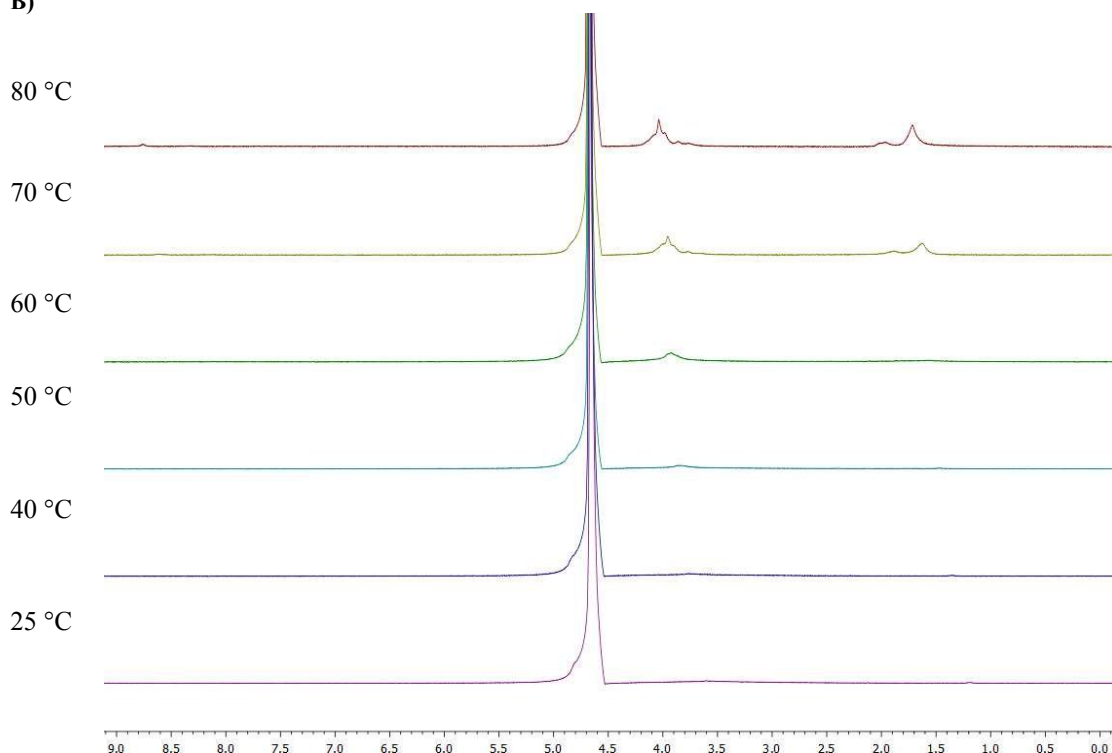


Fig. S8 (A) $^1\text{H-NMR}$ (400 MHz) spectrum of **EG-BTA** in CDCl_3 . $\delta = 8.38$ (s, 3H, Ar), 6.83 (b, 3H, C=ONHCH_2), 3.75-3.53 (m, 48H, $\text{O-(CH}_2)_2\text{-O}$), 3.43 (m, 12H, $\text{CH}_2\text{CH}_2\text{NHC=O}$, $\text{CH}_2\text{CH}_2\text{CH}_2\text{O}$), 2.77 (b, 3H, $\text{CH}_2\text{CH}_2\text{OH}$), 1.67-1.47 (m, 12H, $\text{CH}_2\text{CH}_2\text{CH}_2\text{O}$, $\text{CH}_2\text{CH}_2\text{CH}_2\text{O}$), 1.45-1.15 (m, 45H, aliphatic). The peak at 5.30 corresponds to a trace amount of DCM, which was removed before further use. (B) Variable temperature $^1\text{H-NMR}$ (500 MHz) of **EG-BTA** when cooling down from 80 °C to 25 °C in D_2O ($c = 500 \mu\text{M}$). The signal at 4.79 ppm corresponds to D_2O . At 80 °C broad peaks corresponding to the aliphatic chain (around 1.8 ppm), ethyleneglycol (around 4.0 ppm) and a small peak corresponding to the aromatic group (around 8.5 ppm) were observed. When cooling down, first the aromatic peak disappears (at 70 °C), followed by the peak for the aliphatic chains (at 60 °C). From 40 °C and lower none of the peaks found in CDCl_3 could be observed, indicating that large aggregates have formed. Based on those results, we hypothesize that the assembly process of **EG-BTA** starts from the assembly of the aromatic core and the aliphatic chains before the ethyleneglycol chains are folded around the core of the supramolecular polymer.

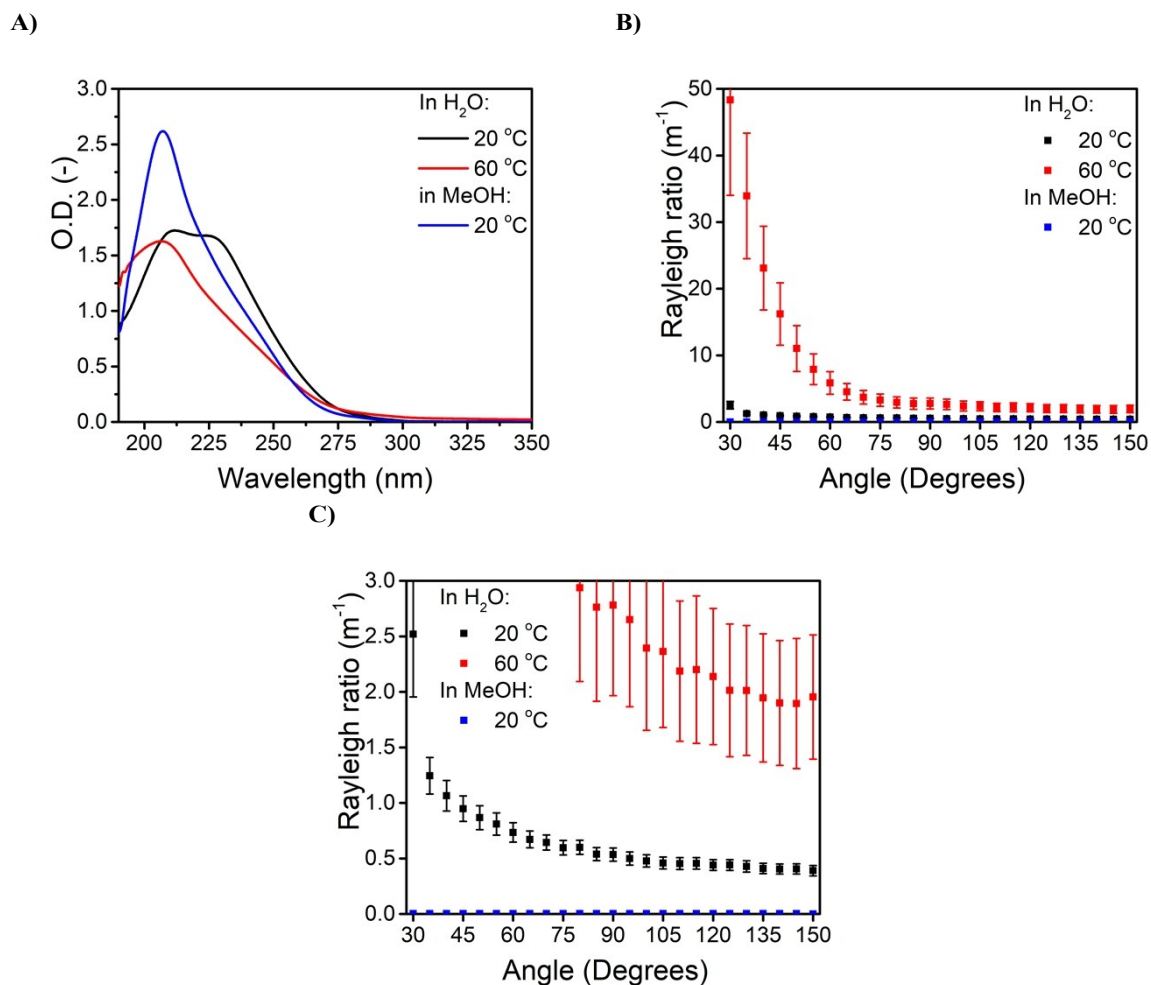


Fig. S9 The change in aggregation state at high temperatures observed for **EG-BTA** in Fig. S5B was studied in more detail. Since the T_{cp} of **EG-BTA** was found at 72 °C we studied the aggregation at a lower temperature, 60 °C. (A) The UV-Vis spectrum of **EG-BTA** ($c = 50 \mu\text{M}$, $l = 1 \text{ cm}$) at 60 °C shows a large maximum at 208 nm, while the spectrum shows two maxima at 212 nm and 226 nm at 20 °C. In MeOH, **EG-BTA** was molecularly dissolved and a large absorption maximum at 207 nm was found. The difference between the UV-Vis spectrum at 60 °C in H₂O and the spectrum in MeOH suggests that **EG-BTA** is not molecularly dissolved at 60 °C. However, the spectrum at 60 °C already shows a slight increase in the absorbance at high wavelengths, indicating that the BTAs have aggregated into larger structures due to the LCST behaviour of the ethyleneglycol. (B) SLS of **EG-BTA** ($c = 582 \mu\text{M}$, $\lambda = 532 \text{ nm}$) at 60 °C shows a large angle-dependent Rayleigh ratio. When compared to the angle-independent Rayleigh ratio in MeOH (see (C) for a zoom), it can be concluded that **EG-BTA** is not molecularly dissolved at 60 °C but instead forms non-spherical aggregates. The increase in the Rayleigh ratio compared to **EG-BTA** at 20 °C confirms that large disordered aggregates are formed at high temperatures. The transition of large disordered aggregates into supramolecular polymers stabilised by hydrogen bonding was also recently demonstrated by coarse grained simulations.⁸

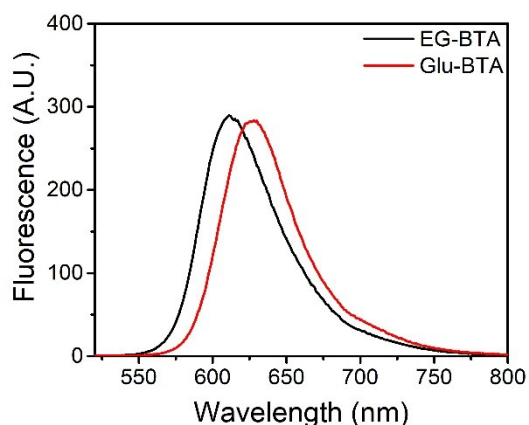


Fig. S10 Fluorescence emission spectra of Nile Red ($c_{\text{Nile Red}} = 2.5 \mu\text{M}$) in solutions of **EG-BTA** and **Glu-BTA** in water ($c_{\text{BTA}} = 50 \mu\text{M}$, $T = \text{room temperature}$, $\lambda_{\text{ex}} = 500 \text{ nm}$, $l = 1 \text{ cm}$).

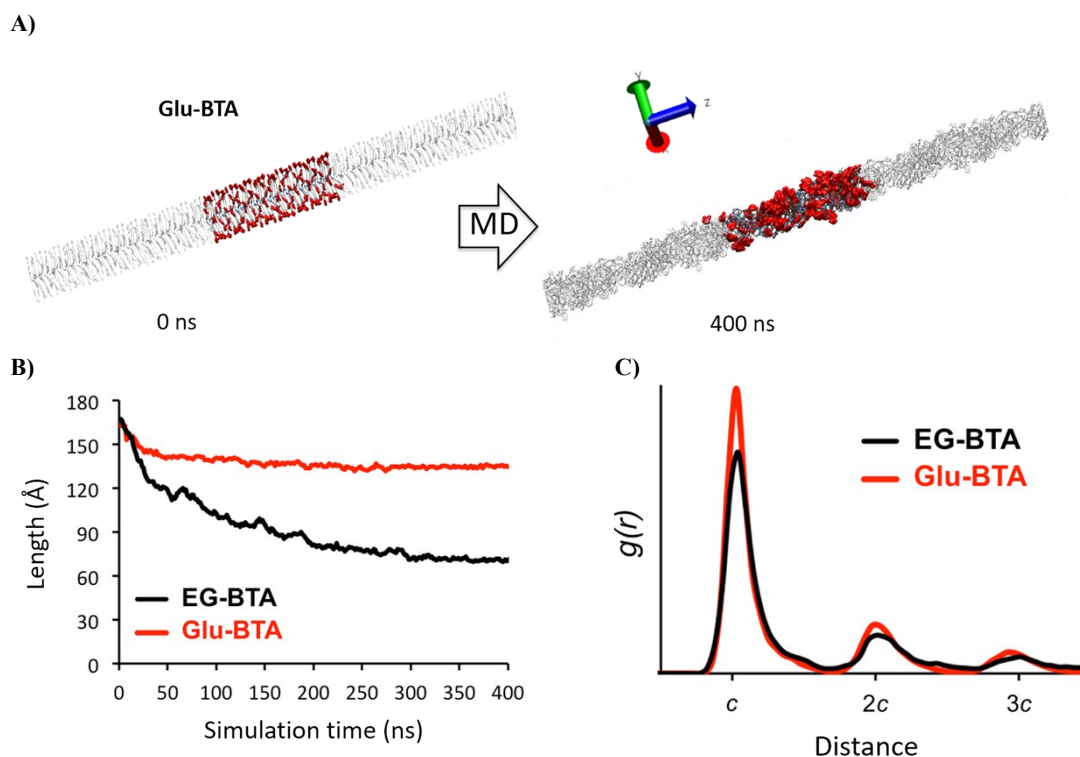


Fig. S11 MD simulation of the **Glu-BTA** fibre in water. (A) Starting and equilibrated (400 ns) configuration of the **Glu-BTA** fibre. In the periodic simulation box, the saccharides are coloured in red (in grey in the periodic box images). (B) Fibre length (box z -size) during the MD simulations of the **EG-BTA** fibres (black) and **Glu-BTA** (red).⁵ (C) Radial distribution functions ($g(r)$) of the cores in equilibrated (last 100 ns of MD) **EG-BTA** (black) and **Glu-BTA** fibres (red).⁵ c corresponds to the intercore distance (3.4 Å).

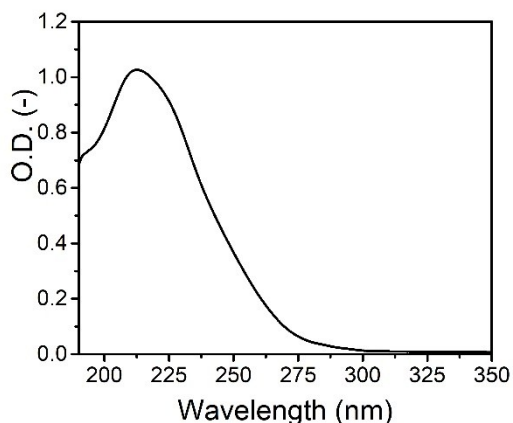


Fig. S12 UV-Vis spectrum of **Glu-BTA** after diluting a 500 μM sample in H_2O 100 times with H_2O to a concentration of 5 μM ($l = 5 \text{ cm}$, $T = \text{room temperature}$). The spectrum matches with the spectrum of **Glu-BTA** before the dilution (Fig. S3A).

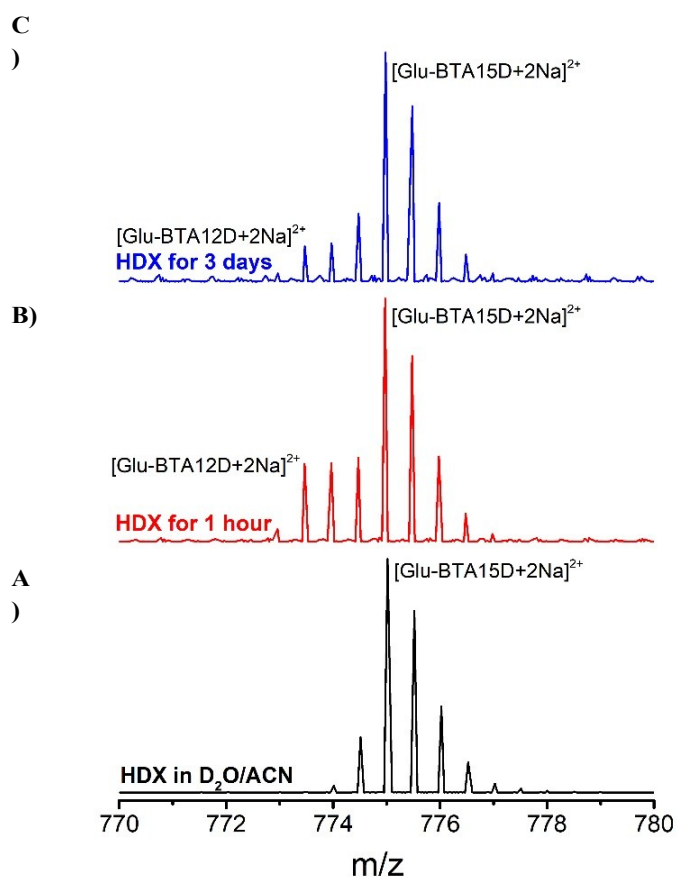


Fig. S13 ESI-MS spectra of **Glu-BTA** taken after dilution (A) in $\text{ACN}/\text{D}_2\text{O}$ showing one isotope distribution corresponding to **Glu-BTA15D**; (B) 1 h after dilution into D_2O showing two dominant isotope distribution corresponding to **Glu-BTA15D** and **Glu-BTA12D** and (C) 3 days after dilution into D_2O showing the **Glu-BTA12D** distribution decrease in intensity.

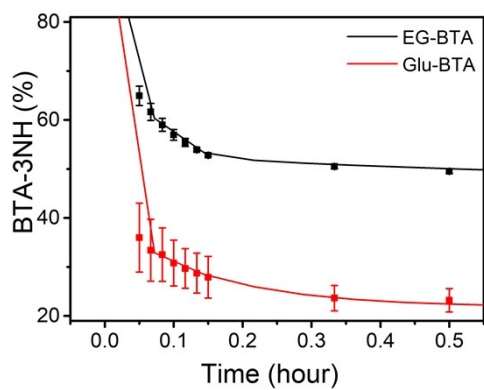


Fig. S14 Zoom of the first 30 minutes of the HDX-MS measurement, showing the faster exchange of **Glu-BTA** as compared to **EG-BTA**. The squares represent the average and the error bars show the standard deviation calculated from three independent measurements. The data was fitted to a tri-exponential fit using Origin 2015.

3. HDX-MS measurements

All HDX-MS experiments of **EG-BTA** and **Glu-BTA** were performed under similar conditions to eliminate influences from the environment, for example temperature. The measurements were performed by diluting a BTA sample in H₂O 100 times into D₂O. UV-Vis spectroscopy confirmed that the assemblies of BTAs do not change due to this drastic decrease in concentration (Fig. S12). The H/D exchange rate depends only on the solvent accessibility of the labile hydrogen atoms, because the acidity of OH and amide-NH is similar (pKa = 14.2 for OH of ethylene glycol,⁹ pKa = 12.5 for OH of α -D-glucose¹⁰ and 13.0 for the benzamide¹⁰). The physical movement of monomers between fibres makes them solvent accessible and this process has previously been proven with STORM and FRET experiments.^{5,11}

Calculating BTA-NH%

Upon diluting a BTA sample into D₂O, all the hydrogen atoms of the OH groups at the periphery will be instantaneously replaced by deuterium atoms leading to the immediate transformation of BTA to BTAmD (m is the number of OH groups at the periphery of a BTA molecule). It was assumed that only the hydrogen atoms of the OH groups exchanged immediately and that the amide NH groups remained unaffected. Therefore, the hypothetical point BTA-3NH = 100% at t = 0 hour was added in Fig. 3. Subsequently, H/D exchange of the three amide groups will take place forming BTA(m+3)D.¹² In calculating the percentage of BTA molecules with the amide hydrogens not exchanged by deuterium atoms, the overlapping isotopic peaks of BTAmD with the peaks of BTA(m+1)D, BTA(m+2)D and BTA(m+3)D, and the presence of 1% H₂O (w/w, with molar ratio of 1.1%), should be taken into consideration.

Considering the presence of 1.1 mol% of H₂O in a HDX solution, all hydrogen atoms (m OH and 3 NH) cannot be completely replaced by deuterium atoms. Statistically, the ratio of

$$\text{BTA}(m+1)\text{D} : \text{BTA}(m+2)\text{D} : \text{BTA}(m+3)\text{D} \text{ is } \binom{m+3}{2} \times 0.011^2 \times (1-0.011)^{(m+3)-2} : \binom{m+3}{1} \times 0.011^1 \times (1-0.011)^{(m+3)-1} : \binom{m+3}{0} \times 0.011^0 \times (1-0.011)^{(m+3)}$$

. This corresponds to a ratio of BTA4D : BTA5D : BTA6D = 1.9x10⁻³ : 6.7x10⁻² : 1 for **EG-BTA** and a ratio of BTA13D : BTA14D : BTA15D = 1.3x10⁻² : 1.7x10⁻¹ : 1 for **Glu-BTA**. In the same way, the ratio of BTA(m-2)D : BTA(m-1)D : BTAmD can be calculated, resulting in BTA1D : BTA2D : BTA3D = 3.8x10⁻⁴ : 3.4x10⁻² : 1 for **EG-BTA** and a ratio of BTA10D : BTA11D : BTA12D = 8.3x10⁻³ : 3.4x10⁻¹ : 1 for **Glu-BTA**. Especially for **Glu-BTA** the presence of 1% H₂O is quite pronounced and cannot be neglected.

Table S1: Theoretical isotope distributions of the doubly charged **EG-BTA-3D** and **Glu-BTA-12D** ions calculated with Bruker Compass IsotopePattern software.

[EG-BTA-3D+2Na]²⁺		[Glu-BTA-12D+2Na]²⁺	
m/z	Relative intensity	m/z	Relative intensity
668.46	1.0	773.46	1.0
668.97	0.77	773.96	0.84
669.47	0.34	774.46	0.39
669.97	0.10	774.97	0.13
670.47	0.03	775.47	0.04

The theoretical isotope distribution of both BTAs is given in Table S1 and it should be kept in mind that the m/z of the isotopes of BTAmD overlaps with the m/z of the BTA(m+1)D, BTA(m+2)D and BTA(m+3)D peaks. Therefore, the contribution from the isotope of BTAmD should be subtracted from the measured intensity of the BTA(m+1)D, BTA(m+2)D and BTA(m+3)D peaks to correct the intensity for the overlap of the isotopes.

Based on the discussion above, BTAmD% is calculated by the following equation:

$$\text{BTAmD\%} = \frac{I_{\text{BTAmD}}}{I_{\text{BTA}(m-1)\text{D}} + I_{\text{BTAmD}} + (I_{\text{BTA}(m+3)\text{D}} - p \times I_{\text{BTAmD}}) + (I_{\text{BTA}(m+2)\text{D}} - q \times I_{\text{BTAmD}})} \times 100\% \quad (2)$$

where I_{BTAmD} , $I_{\text{BTA}(m-1)\text{D}}$, $I_{\text{BTA}(m+3)\text{D}}$, $I_{\text{BTA}(m+2)\text{D}}$ and $I_{\text{BTA}(m+1)\text{D}}$ represent the intensities of the monoisotopic peaks for the doubly sodiated ions of BTAmD, BTA(m-1)D, BTA(m+3)D, BTA(m+2)D and BTA(m+1)D, and p, q and r represent the relative isotopic peak intensity of the isotopes of BTAmD at the same m/z as the monoisotopic peaks of the doubly sodiated ions of BTAmD as shown in Table S1 (corresponding to p = 0.10, q = 0.34 and r = 0.77 for **EG-BTA** and p = 0.13, q = 0.39 and r = 0.84 for **Glu-BTA**).

Discussion on solvent penetration during the HDX-MS experiments

As discussed above, the presence of a trace amount of H₂O implies that not all labile hydrogen atoms can be replaced by deuterium atoms. Therefore, BTA(m+1)D, BTA(m+2)D and BTA(m-1)D species will always be present in the sample. Moreover, when single D₂O molecules would penetrate the hydrophobic pocket and reach the core amide hydrogen atoms these would exchange individually instead of simultaneously (when the monomer is released into the bulk solvent). This would also cause the formation of BTA(m+1)D (BTA-4D for **EG-BTA** and BTA-13D for **Glu-BTA**) and BTA(m+2)D (BTA-5D for **EG-BTA** and BTA-14D for **Glu-BTA**). To analyse this process, we plotted the percentage of the different species present in the solution as a function of time for both assemblies (Fig. S15A and S15B). It is shown in those plots that especially in the first hour there is quite some BTA(m+1)D and BTA(m+2)D present. In Fig. S15C and S15D we have made this even more evident by plotting the ratios between different deuterated species against the theoretical ratio calculated from the trace

amount of water expected to be in the D₂O based on the dilution of the BTA sample. Especially in the first hour after the dilution step there is a large discrepancy between the experiments and the theory, which we assign to the penetration of D₂O into the hydrophobic pocket of the BTAs fibres, leading to the individual H/D exchange of amide hydrogen atoms. Since the ratios seem to stabilize after one hour, we expect that the contribution of D₂O penetration to the H/D exchange minimalizes after that time. The ratios after one hour are still higher than predicted, which might be due to the penetration of the trace amount of H₂O into the hydrophobic pocket, causing back exchange of deuterium atoms into hydrogen atoms. Since also the ratio of BTA(m-1)D/BTA_mD is higher than calculated, we hypothesize that there is more water present in our D₂O than expected at first hand due to exchange with the air.

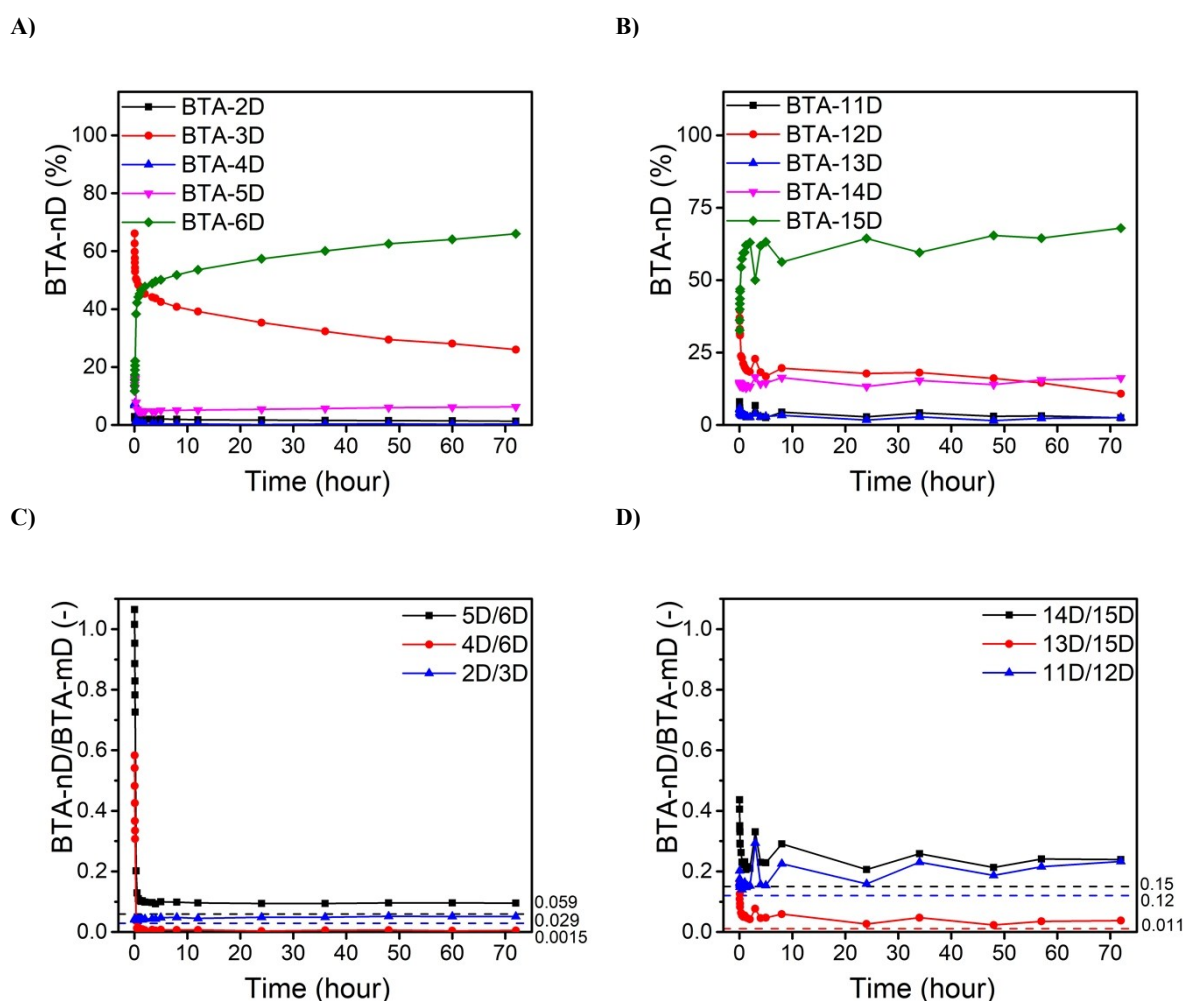


Fig. S15 (A) The percentage of the different deuterated species of **EG-BTA** during a single HDX-MS experiment as a function of time after diluting a 500 μ M sample 100 times into D₂O. (B) The percentage of the different deuterated species of **Glu-BTA** during a single HDX-MS experiments as a function of time after diluting a 500 μ M sample 100 times into D₂O. The variation between the measurement points might be caused by a more complicated ESI process. (C) Ratios between different deuterated species of **EG-BTA** as a function of time. The dotted lines show the theoretical values for the three ratios. (D) Ratios between different deuterated species of **Glu-BTA** as a function of time. The dotted lines show the theoretical values for the three ratios.

Fitting BTA-NH% to a tri-exponential fit

The percentage of BTAmD was plotted over time and the data for **EG-BTA** and **Glu-BTA** was fitted to a tri-exponential fit using Origin 2015. Using the Fitting Function Builder, the equation $\text{BTAmD}\% = A \cdot \exp(-t \cdot b) + C \cdot \exp(-t \cdot d) + E \cdot \exp(-t \cdot f)$ was created with A, b, C, d, E and f being the parameters that were varied during the fitting and t (time in hours) being the independent variable. The data for **EG-BTA** was fitted to $\text{BTA3D}\% = 46.89 \cdot \exp(-t \cdot 24.75) + 8.29 \cdot \exp(-t \cdot 0.79) + 44.66 \cdot \exp(-t \cdot 0.0089)$ ($R^2_{\text{adj}} = 0.9983$) and the data for **Glu-BTA** was fitted to $\text{BTA12D}\% = 61.00 \cdot \exp(-t \cdot 69.75) + 17.16 \cdot \exp(-t \cdot 6.59) + 21.85 \cdot \exp(-t \cdot 0.0069)$ ($R^2_{\text{adj}} = 0.9988$). The residuals of the fit are shown in Fig. S16.

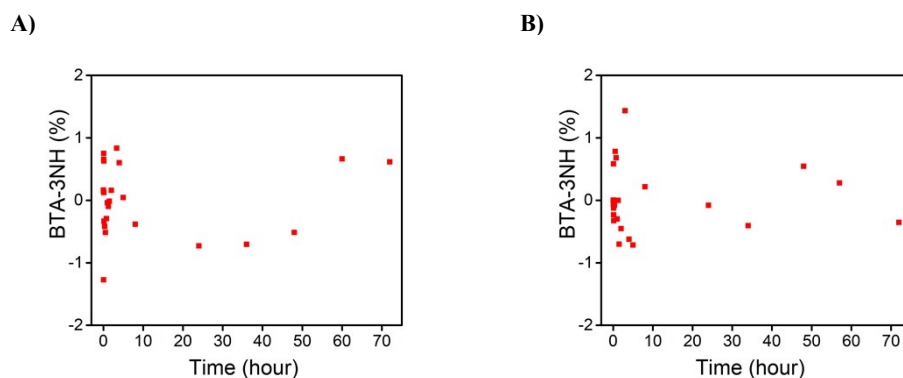


Fig. S16 Residuals of the tri-exponential fit of **EG-BTA** (A) and **Glu-BTA** (B) when the HDX-MS data is fitted to a tri-exponential fit with Origin 2015.

4. Molecular dynamics simulations

The entire simulation work was conducted using the AMBER 12 software.¹³ The atomistic model for the **Glu-BTA** fibre was built according to the same procedure used in our recent works on **EG-BTA** ones.^{5,14,15} The **Glu-BTA** monomer was parameterized with the “general AMBER force field (GAFF)” (*gaff.dat*).¹⁶ The initial **Glu-BTA** fibre model was built starting from 48 self-assembled pre-stacked cores (configuration obtained replicating along the main fibre axis BTA core stacks previously optimized by density functional theory (DFT) calculations: intercore distance of 3.4 Å),¹⁷ on which we mounted the extended C₁₂-triazole-glucose chains. The molecular model for the **Glu-BTA** fibre was immersed in a periodic simulation box containing explicit TIP3P water molecules,¹⁸ built in such a way that the **Glu-BTA** fibre replicates to the infinite along the *z*-axis (main axis of the fibre) via periodic boundary conditions. As such, the molecular model replicated in space is representative of a section of the bulk of an ideal (monodisperse) **Glu-BTA** fibre of infinite length in water. This initial configuration for the **Glu-BTA** fibre is identical to that of **EG-BTA** fibres we simulated recently,^{5,14} with the unique difference of the saccharide-functionalized side chains.

After initial minimization, the systems initially underwent 50 ps of heating MD simulation in NVT conditions (constant N: number of atoms, V: volume, and T: temperature in the system) to reach the experimental temperature of 20 °C (293 K), during which the solute was kept fixed. Following to the same simulation protocol reported recently for **EG-BTA** fibers,⁵ the restraints were removed from the lateral chains, and the **Glu-BTA** fibre was pre-equilibrated for other 2 ns of MD simulation in NPT conditions (constant N: number of atoms, P: pressure, and T: temperature in the system) at room temperature (T = 20 °C) and 1 atm of pressure. This phase allowed the lateral chains to pre-relax around the fibre core. Finally, all restraints were removed and the systems underwent 400 ns of MD simulation in NPT conditions at room temperature (T = 20 °C) and 1 atm of pressure. Due to the anisotropic (1D) nature of the simulated fibre models, anisotropic pressure scaling was adopted in order to allow the fibre to rearrange and fold during the MD run. In the MD, a time step of 2 femtoseconds, the Langevin thermostat, and a 10 Å cutoff were used.^{5,14} The particle mesh Ewald¹⁹ approach (PME) was used to treat the long-range electrostatics. All bonds involving hydrogen atoms were treated with the SHAKE algorithm.²⁰ The fibre length, the root mean square displacement (RMSD) and the fibre energy data were used to assess the equilibration of the simulated systems in the MD regime. The fibre was observed to reach the equilibrium after ~250 ns of MD (*e.g.*, Fig. S11B). The last 100 ns of MD were considered as representative of the equilibrated **Glu-BTA** fibre and were used for the analysis. The structural and hydrogen bonding analyses were conducted with the *ptraj* module of AMBER 12. The length of the fibre model was monitored directly from the box size in *z*-direction (main fibre axis).^{5,14}

5. References

- 1 C. M. A. Leenders, L. Albertazzi, T. Mes, M. M. E. Koenigs, A. R. A. Palmans and E. W. Meijer, *Chem. Commun.*, 2013, **49**, 1963.
- 2 C. M. A. Leenders, G. Jansen, M. M. M. Frissen, R. P. M. Lafleur, I. K. Voets, A. R. A. Palmans and E. W. Meijer, *Chem. - A Eur. J.*, 2016, **22**, 4608–4615.
- 3 J. Wang, I. K. Voets, R. Fokkink, J. van der Gucht and A. H. Velders, *Soft Matter*, 2014, **10**, 7337–45.
- 4 Z. Osváth and B. Iván, *Macromol. Chem. Phys.*, 2017, **218**, 1–13.
- 5 M. B. Baker, L. Albertazzi, I. K. Voets, C. M. A. Leenders, A. R. A. Palmans, G. M. Pavan and E. W. Meijer, *Nat. Commun.*, 2015, **6**, 6234.
- 6 J. S. Pedersen and P. Schurtenberger, *Macromolecules*, 1996, **29**, 7602–7612.
- 7 C. M. A. Leenders, M. B. Baker, I. A. B. Pijpers, R. P. M. Lafleur, L. Albertazzi, A. R. A. Palmans and E. W. Meijer, *Soft Matter*, 2016, **12**, 2887–2893.
- 8 D. Bochicchio and G. M. Pavan, *ACS Nano*, 2017, **11**, 1000–1011.
- 9 Dissociation Constants of Organic Acids and Bases,
https://labs.chem.ucsb.edu/zhang/liming/pdf/pKas_of_Organic_Acids_and_Bases.pdf.
- 10 Dissociation constants of organic acids and bases,
[http://sites.chem.colostate.edu/diverdi/all_courses/CRC reference data/dissociation constants of organic acids and bases.pdf](http://sites.chem.colostate.edu/diverdi/all_courses/CRC_reference_data/dissociation_constants_of_organic_acids_and_bases.pdf).
- 11 L. Albertazzi, R. W. Van Der Hofstad and E. W. Meijer, *Science*, 2014, **491**, 10–15.
- 12 X. Lou, R. P. M. Lafleur, C. M. A. Leenders, S. M. C. Schoenmakers, N. M. Matsumoto, M. B. Baker, J. L. J. van Dongen, A. R. A. Palmans and E. W. Meijer, *Nat. Commun.*, 2017, **8**, 15420.
- 13 R. D.A. Case, T.A. Darden, T.E. Cheatham, III, C.L. Simmerling, J. Wang, R.E. Duke, G. S. Luo, R.C. Walker, W. Zhang, K.M. Merz, B. Roberts, S. Hayik, A. Roitberg, J. L. J. Swails, A.W. Götz, I. Kolossváry, K.F. Wong, F. Paesani, J. Vanicek, R.M. Wolf, G. X. Wu, S.R. Brozell, T. Steinbrecher, H. Gohlke, Q. Cai, X. Ye, J. Wang, M.-J. Hsieh and P. A. K. Cui, D.R. Roe, D.H. Mathews, M.G. Seetin, R. Salomon-Ferrer, C. Sagui, V. Babin, T. Luchko, S. Gusarov, A. Kovalenko, *AMBER 12*, 2012, University of California, San Francisco.
- 14 M. Garzoni, M. B. Baker, C. M. A. Leenders, I. K. Voets, L. Albertazzi, A. R. A. Palmans, E. W. Meijer and G. M. Pavan, *J. Am. Chem. Soc.*, 2016, **138**, 13985–13995.
- 15 D. Bochicchio, M. Salvalaglio and G. M. Pavan, *Nat. Commun.*, 2017, **8**, 147.
- 16 J. M. Wang, R. M. Wolf, J. W. Caldwell, P. a Kollman and D. a Case, *J. Comput. Chem.*, 2004, **25**, 1157–1174.
- 17 I. A. W. Filot, A. R. A. Palmans, P. A. J. Hilbers, R. A. Van Santen, E. A. Pidko and T. F. A. De Greef, *J. Phys. Chem. B*, 2010, **114**, 13667–13674.
- 18 W. L. Jorgensen, J. Chandrasekhar, J. D. Madura, R. W. Impey, M. L. Klein, W. L. Jorgensen, J. Chandrasekhar, J. D. Madura, R. W. Impey and M. L. Klein, , DOI:10.1063/1.445869.
- 19 T. Darden, D. York and L. Pedersen, *J. Chem. Phys.*, 2001, **10089**, 10089–10092.
- 20 V. Kräutler, W. F. Van Gunsteren and P. H. Hünenberger, *J. Comput. Chem.*, 2001, **22**, 501–508.